Title

Voltage-Based Strategies for Preventing Battery Degradation under Diverse Fast-Charging Conditions

Journal

ACS Energy Letters, 8(10)

ISSN

2380-8195

Authors

Konz, Zachary M

Weddle, Peter J

Gasper, Paul

et al.

Publication Date

2023-10-13

DOI

10.1021/acsenergylett.3c01591

Voltage-based strategies for preventing battery degradation under diverse fast-charging conditions

Zachary M. Konz[1,2,3], Peter J. Weddle[1], Paul Gasper[1], Bryan D. McCloskey[2,3], Andrew M. Colclasure[1]

1. Energy Conversion and Storage Systems Center, National Renewable Energy Laboratory, Golden, CO, USA
2. Department of Chemical and Biomolecular Engineering, University of California, Berkeley, Berkeley, CA, USA
3. Energy Storage and Distributed Resources Division, Lawrence Berkeley National Laboratory, Berkeley, CA, USA

Abstract

Maintaining safe operating conditions is a key challenge for high-performance lithium-ion battery applications. The lithium plating reaction remains a risk during charging, but limited studies consider the highly variable charging conditions possible in commercial cells. Here we combine pseudo-2D electrochemical modeling with data visualization methods to reveal important relationships between the measurable cell voltage and difficult-to-predict Li plating onset criteria. An extensively validated model is used to compute lithium plating for thousands of multistep charging conditions spanning diverse rates, temperatures, states-of-charge (SOC), and cell aging. We observe an empirical cell operating voltage limit below which plating does not occur across all conditions, and this limit varies with battery state-of-charge and aging. A model sensitivity analysis also indicates that when comparing two charging voltage profiles, the capacity difference at 4.0V correlates well with the difference in the plating onset capacity. These results encourage simple strategies for Li plating prevention that are complementary to existing battery controls.

Main Text

Lithium-ion batteries are central to the global energy transition, and fast-charging technology may have broad impacts for their utilization beyond obvious performance improvements. One example pertains to electric vehicle design. Vehicles are increasingly designed with large battery packs and long ranges (>300 km) to reduce the frequency of inconvenient charging[1]. With widespread fast-charging, however, this trend could be reversed, leading to battery material conservation and more affordable vehicles that still satisfy the daily driving habits of most consumers.

On the individual battery cell level, the primary limitation for fast-charging is the poorly reversible lithium plating reaction that occurs instead of desired graphite intercalation. Understanding of the intertwined physical phenomena that can cause Li plating has progressed over decades[2–6]. While plating is frequently studied in the context of fast-charging of high-power cells (80% charge in <15 minutes), it is equally a concern for low-temperature charging[7], cell aging conditions[6,8], and moderate charging of high-energy cells[9,10].

Recent battery operating advances to enable fast-charging have focused on charge protocol development and control systems that prevent lithium plating by preventing the graphite potential from passing below the Li plating limit (0 V vs. Li/Li^+)[11,12]. Common strategies for charge protocol discovery include Doyle-Fuller-Newman (DFN) based electrochemical modeling[13], the use of three-electrode experiments[14–16], and data-driven methods[17,18]. For real-time battery controls, model predictive control (MPC) methods effectively apply constraints from the DFN model[19] to enhance charging performance and safety. The promise of the MPC approach has led to diverse efforts to reduce its high computational cost[20–25], typically via some combination of approximating the complex DFN model and simplifying the controls schemes with added elements such as reference governors[20,21,23].

A remaining challenge not reflected in many studies is that realistic battery charging conditions vary widely and depend on factors such as application, charging infrastructure, climate, energy availability and pricing, consumer needs, and pack configuration. Optimal charging protocols and temperature management vary across applications. The initial battery temperature will vary greatly by climate. Temperature rise during charge can be rapid at the cell level and increases with rate[26], energy density, and can exceed 20°C/min depending on the pack configuration and thermal management[27]. Novel shape memory alloy wires that facilitate rapid switching between battery insulation and cooling during fast charge[28] highlight system design factors. Additional challenges that emerge at the pack level include uneven cell aging[29] and temperature variability that can cause aging in colder cells linked to Li plating[30]. This diverse behavior might be captured with cell-level controllers, diagnostic testing, or temperature probes, but these add substantial computational or hardware cost.

In this work, we use electrochemical modeling and data visualization methods to explore simple voltage-based strategies to prevent fast-charging degradation over diverse conditions. First, we

leverage recent experimental advances to quantify Li plating[31] to calibrate a high-fidelity electrochemical Li plating model and add modifications to reflect battery aging. Then we simulate fast charging while systematically changing operating or aging parameters, and quantify the relationship between measurable voltage characteristics and the plating onset response. Finally, we devise an algorithm for generating realistic, coupled current-temperature charging protocols, and use simulation results to propose empirical operating voltage constraints to safely avoid plating. Together, the findings reveal important connections between real-time voltage measurements and fast-charging ability that could reduce the negative impact of cell variability on performance.

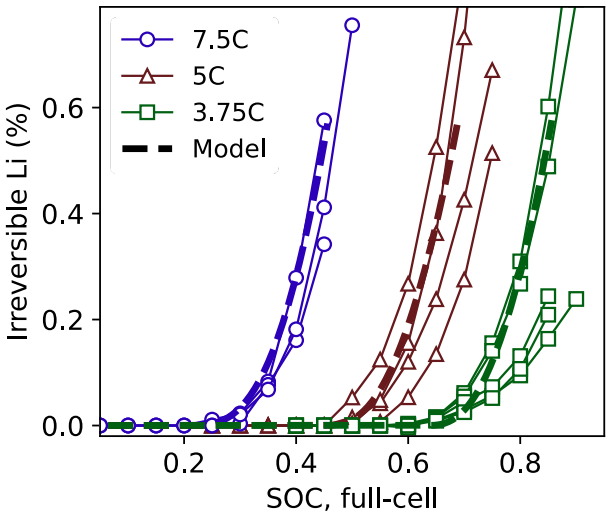

Fig. 1 | Calibrated model output for Li plating compared with Ref. 31 experimental data. The results are for Gr|NMC532 cells at T=30°C and constant current charge, where 1C = 2.8 mA/cm^2. Irreversible Li plating capacity is reported as a percentage of the graphite capacity, 3.35 mAh/cm^2.

This study employs a pseudo-2D (P2D) electrochemical-thermal model of a Graphite|$LiNi_{0.5}Mn_{0.3}Co_{0.2}O_2$ (NMC532) cell that has extensive experimental validation for fast charging and lithium plating. Early works[5,32] show strong model-experiment agreement for charging voltage profiles at varying electrode loadings (1.5 to 5.0 mAh/cm^2), currents (1C to 9C), and temperatures (20 to 50°C)[32]. Experimental Li plating quantification in Li|Graphite half-cells was then used to estimate an exchange current density (i_0) for the lithium plating reaction[33] and refine the expression for lithium diffusion in graphite particles[31]. Finally, in this work, the P2D model was recalibrated to Li plating results of a 2.8 mAh/cm^2 cell from Ref. 31 by matching the reported material properties (Table S2) and doubling the graphite exchange current density pre-factor. This change increases the maximum i_0 from about 5 to 10 A/m^2 at standard Li concentrations and 30°C, well within literature ranges[34,35]. The model gives the expected lithium plating response to changes in rate (Fig. 1) and temperature (Fig. S1).

Li plating sensitivity to aging and operating parameters

We then utilize the calibrated P2D model to quantify the impact of aging on fast-charging performance and lithium plating. This is in response to widespread recognition of the importance of cell aging on plating but a dearth of studies due to the difficulty of experimental data collection and model validation. Here we add simple and physical aging mechanisms to our model formulation, summarized in Table 1. The equation adjustments new to this work are shown in the supplementary information and complement past model documentation from Ref. 36. We approximate the worst values of each parameter under the assumption that cells with less than 80% of the initial capacity are not likely used for high-performance applications. Thus, we expect that up to 10-20% change in the values is possible for operational cells. The exception is the charge transfer kinetics parameters, which may change to a greater extent due to knowledge that reaction

Table 1 | Aging mechanisms and values applied to Li plating model

Aging mechanism	Description	Value Range (Best – Worst)	Max. range expected within battery pack
Electrode expansion	The electrode thickness is increased and a void fraction is created, decreasing the volume fraction of other components (electrolyte, solids) and increasing the spacing between particles	0 – 8 µm, anode 0 – 8 µm, cathode	4 µm 4 µm
Void formation or electrolyte depletion	A void fraction is subtracted from the electrolyte volume fraction (porosity) is decreased, also affecting tortuosity, while other component fractions remain unchanged	0 – 0.05, anode 0 – 0.05, cathode	0.03 0.03
Loss of active material	The active material fraction of the total electrode solids is decreased, decreasing the electrode capacity and active reaction surface area	0 – 10%, anode 0 – 20%, cathode	6% 15%
Charge transfer kinetics decrease	The exchange current density is multiplied by a coefficient (≤ 1), increasing the resistance to charge transfer	1 – 0.5, anode 1 – 0.5, cathode	0.4 0.4
Lithium inventory loss, slippage	The anode lithiation at the start of charge is decreased relative to the expected value given the cathode lithiation	0 – 0.08*, anode	0.05
Electrolyte conductivity decrease	The electrolyte conductivity is multiplied by a coefficient (≤ 1)	1 – 0.8, electrolyte	0.2

See Supplementary Information for model formulation of each mechanism. The initial electrode lengths are ~70μm and electrolyte volume fractions ~0.35. *For charges starting at low SOC, this value is constrained such that ($x \geq 0.01$ in Li_xC_6).

kinetics can change orders of magnitude with surface passivation. The final column in Table 1 estimates the largest cell-to-cell variability of each parameter at a given moment throughout the battery pack's lifetime and will be used for the analysis of Fig. 3. Justification for the mechanisms and values selected is in the Supplementary Information, but these will vary by application or chemistry so the emphasis herein is placed on the broadly transferable workflow and results.

Fig. 2 visualizes the effect of various operating and aging parameters on the charging voltage curve and Li plating onset for constant-current, constant-temperature charging. The *x*-axis for these plots is the normalized charge capacity delivered so all curves begin at x=0. Battery temperature and rate have outsize impact on the voltage and Li plating onset, shown in Fig. 2a-b where the plating onset is marked by stars, as expected from many past works[5,31–33]. Plating is known to become more likely at higher states-of-charge (SOC) as the graphite approaches its full lithiation capacity, so it logically follows that increasing the initial state-of-charge (SOC) leads to plating at earlier charge capacities (Fig. 2c). Conversely, the loss of lithium inventory (LLI) in the graphite electrode lowers the initial lithiation relative to the expected value and more charge capacity can be safely delivered before plating (Fig. 2j, stars shift right from the baseline). LLI is the only aging mechanism that interestingly postpones the Li plating onset. The aging most drastically affecting plating is related to decreased Li-ion electrolyte transport within the graphite via void formation or expansion (Fig. 2d-e), although these changes minimally affect the full-cell voltage. The voltage profiles are more affected by changes to the NMC electrode (Fig. 2f,l) due the sensitivity of its potential to lithiation state. Graphite intercalation kinetics worsening may also critically affect lithium plating if the exchange current value decreases greater than 50% (Fig. 2g).

Correlating the voltage response and plating onset

Next, we systematically quantify the relationship between voltage change and plating onset change from Fig. 2. The goal of this analysis is to understand whether voltage profile variability between cells, measured at the beginning of charge, can give accurate, cell-specific Li plating onset predictions later during the same charge. Fig. 3a illustrates the two metrics we use to quantify the difference between voltage curves: the average capacity difference between 3.95-4V (ΔQ_{4V}) and

the average voltage difference between 2-5% capacity ($\Delta V_{2\text{-}5\%}$). These regions were selected because Li plating is not expected until well beyond 4V or 5% charge capacity for all conditions; lower voltage regions (< 3.95V) were not considered because some conditions start at high SOC and thus high cell voltage (> 3.85V), and lower capacity regions (< 2%) were not selected because voltage differences are smaller in magnitude at the start of charge. Similarly, the change in plating onset voltage and capacity, which would be useful quantities to predict for battery control systems, is annotated in Fig. 3a. Figs. 3c-f plot the correlation between these voltage and plating onset metrics for the physical parameters labeled in Fig. 3b. Each data point is generated from a unique combination of 2 curves from a given panel of Fig. 2 where the parameter difference is below the values in Table 1 or Fig. 3 caption. The maximum parameter difference constraint is applied because we seek to analyze small deviations in cell voltage within a nominally uniform pack at a single condition, not the voltage change spanning all possible battery conditions.

The first interesting conclusion drawn from this analysis is that Li plating prediction models should be designed to predict the onset SOC or capacity instead of the onset voltage. Figs. 3c-d show

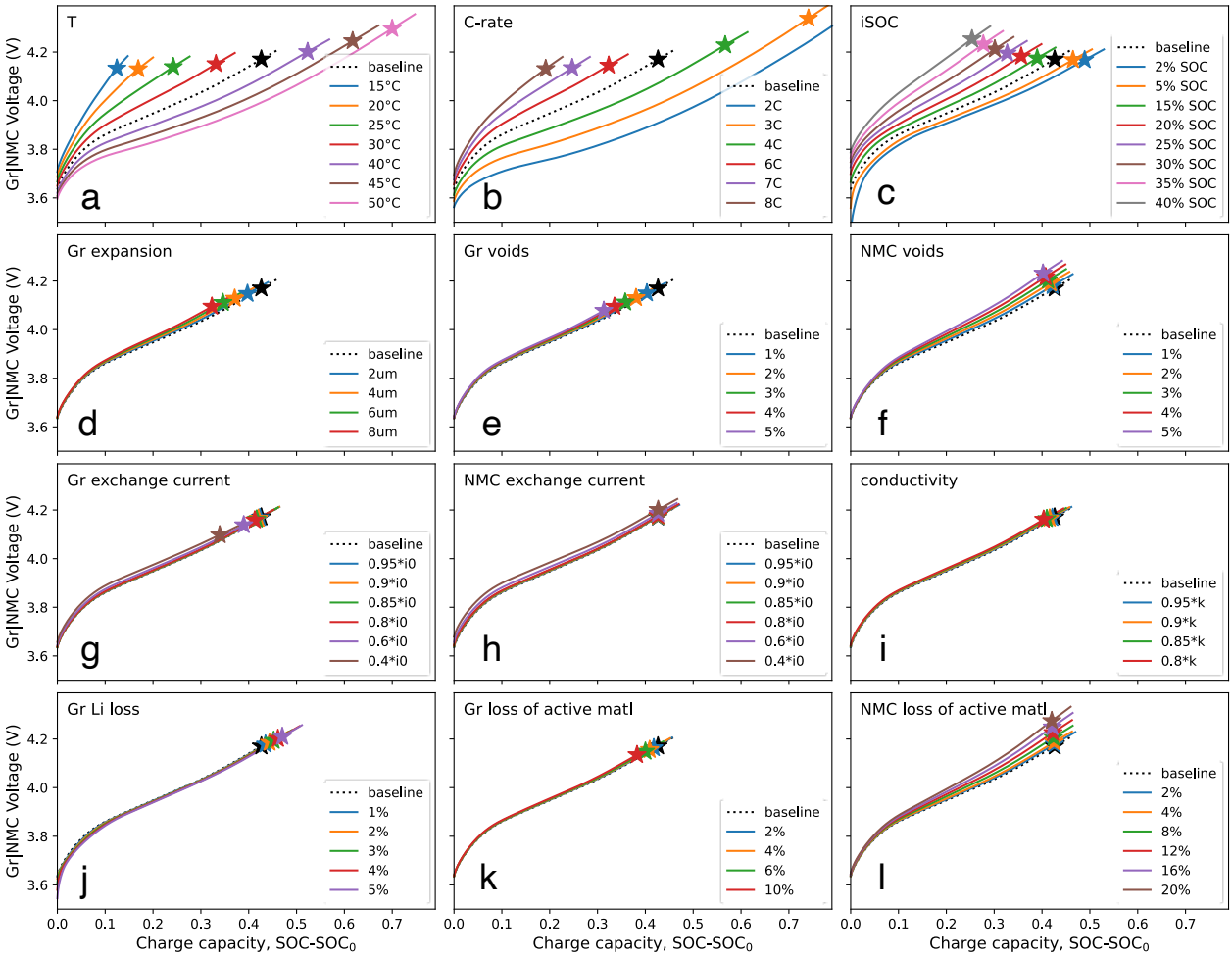

Fig. 2 | Voltage and Li plating sensitivity to operating parameters and aging conditions. The baseline condition is constant-current charging at 5C, 35ºC, 10% initial SOC, and no aging. Each panel shows the effect of a single parameter on the baseline voltage profile and Li plating onset (star). The Li plating onset is defined as the point where irreversible Li plating amount exceeds 0.01% of the graphite capacity (3.35 mAh/cm^2).

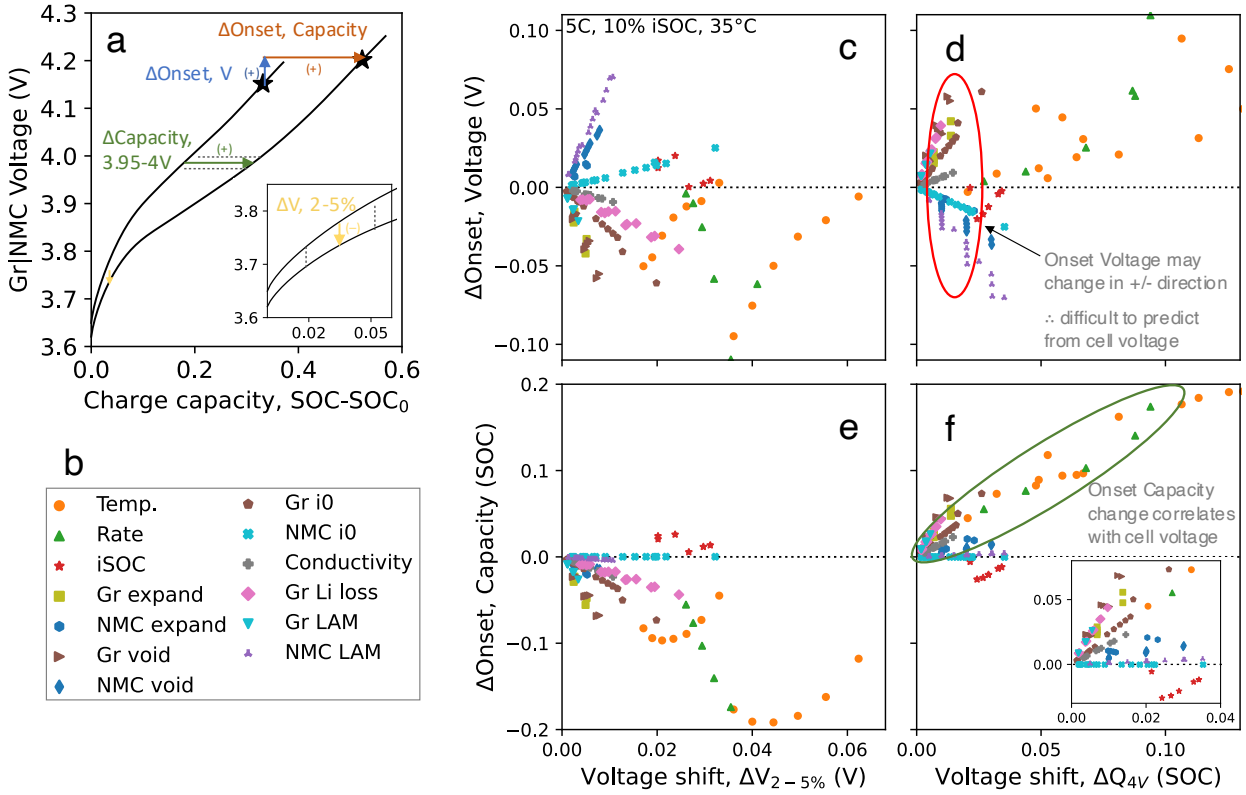

Fig. 3 | Quantifying the correlation between voltage shift and Li plating onset change for the physical phenomena of Fig. 2. a, Two metrics are used to quantify the shift in voltage curve: the average voltage change between 2-5% charge capacity ($\Delta V_{2\text{-}5\%}$, yellow arrow) and the average capacity (SOC) change between 3.95-4.00V (green arrow). The plating onset change is quantified by the change in onset voltage or onset capacity, corresponding to the lengths of the respective arrows. **b,** Legend for data in panels c-f specifying which physical parameter causes the response. **c-f,** Each axis corresponds to one of the metrics in (a). Each data point is calculated from a unique combination of voltage curves from Fig. 2 that have the same parameter varied within the 'Maximum range expected within battery pack' of Table 1. The maximum variability for temperature, rate, and initial SOC (iSOC) are taken to be 10ºC, 1C, 5% respectively. It follows, then, that there are 13 temperature data points in each panel for the following simulation pairs [ºC-ºC] of Fig. 2: [15-20], [15-25] , [20-25], [20-30], [25-30], [25-35], [30-35], [30-40], [35-40], [35-45], [40-45], [40-50], [45-50].

points scattered both above and below the y=0 line, indicating that for a given shift in the voltage profile (x-axis value), the plating onset voltage (y-axis value) could change in the positive or negative direction (Fig. 3d, red oval) depending on the underlying parameter change, making it difficult to predict. This means that additional knowledge of the specific aging mechanisms would be required to make an accurate onset voltage prediction. In contrast, data points for Figs. 3e-f that plot the change in onset capacity largely fall on the same side of the y=0 line. For Fig. 3e, this observation is readily interpretable. For a positive voltage shift corresponding to increased cell resistance due to lower temperature, for example, the plating onset capacity is shifted earlier, as indicated by the negative values. Most interestingly, the ΔQ_{4V} voltage metric correlates exceptionally well with the change in onset capacity regardless of underlying physical phenomena. These findings hold when the Figs. 2 and 3 analysis is repeated at different baseline conditions of [4C, 25ºC, 20% SOC] and [7C, 45ºC, 5% SOC], shown in Figs. S2-3.

The sensitivity analysis workflow of Figs. 2 and 3 provides important insights towards battery management system (BMS) development and generally demonstrates the power of high-fidelity

P2D models for battery systems. The ΔQ_{4V} metric may be a promising input for a voltage-based machine learning model that predicts the Li plating onset capacity. However, the data points from the NMC exchange current density variation (NMC i_0, blue x) lay along the y=0 line of Fig. 3f, indicating that this aging mechanism could cause a "false-positive" event in which the voltage shifts but Li plating onset capacity is unchanged. Similarly, the initial SOC variation yields points below the y=0 line (red stars), contradicting the trend of the other parameters (green oval). These observations highlight the importance of other BMS diagnostics, aging models, and SOC estimators to enhance a purely voltage-based model to enable safe high-performance fast charging.

Meta-analysis across variable charging conditions

We then wanted to understand Li plating behavior and fast-charging limitations over the vast current and temperature combinations that may be experienced by large format cells. There are recent reports of combined charging protocol and thermal management synergies[28,37], but the design space remains mostly unexplored because typically model users specify a current protocol and compute the heat generation for only a single thermal management condition. For P2D models of single-layer cells like ours, this approach predicts low battery self-heating (< 7°C at 7.5C rate) relative to multi-layer commercial cells. For 3D models that might fill this gap, there is increased computational complexity and uncertainty due to the difficulty of model calibration. Here, we instead impose time-dependent piecewise temperature and current functions on the P2D model, striving to simulate conditions realistic to commercial cells under diverse thermal management strategies. Table 2 shows parameters used to constrain the randomly generated fast-charging conditions to plausible SOC, currents, temperatures, and temperature ramps. Figs. 4a-b shows examples

Table 2 | Parameters for generating realistic fast charging conditions

Variable	Value
Number of current steps	4
Stop SOC	0.95
Initial SOC [min,max]	[0.02, 0.5]
[Min, Max] rates by step	Max: [8, 7, 6, 5]C Min: [3, 3, 2, 2]C
[Min, Max] temperature ramp at I_{ref} = 8C	[5, 20] °C/min
[Min, Max] initial charging temperature	[10, 45] °C
[Min, Max] target temperature of charge	[30, 60] °C
Minimum difference between target and initial temperature	5 °C
Temperature drift factor max	0.2
Max rate increase for final current step	0.5 C

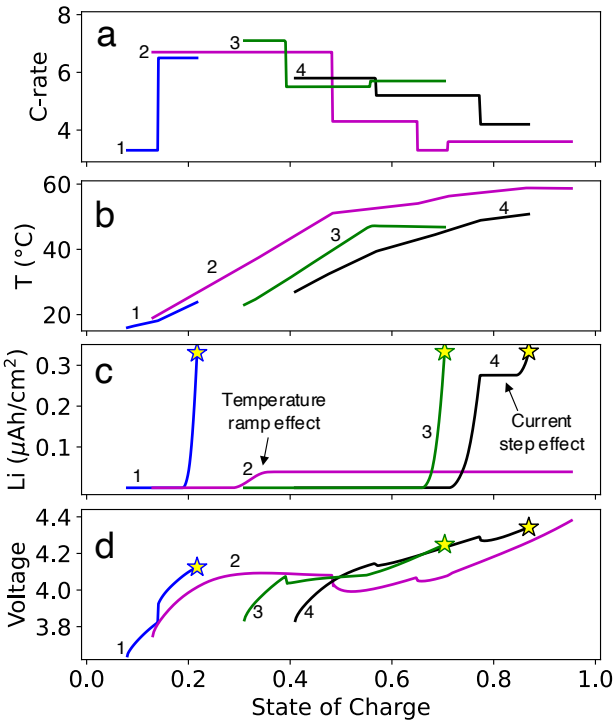

Fig. 4 | Visualizing model Li plating and voltage output for example fast charging simulations. a, Normalized current (1C = 2.8 mA/cm^2) and **b,** Temperature profiles applied to the fast charging model, with **c,** simulated total irreversible Li plating and **d,** simulated Gr|NMC cell voltage. Data are displayed either until the Li plating onset condition is met (curves 1,3,4), denoted by the stars, or until the cell voltage reaches 4.40V (curve 2). Each fast-charging protocol generated with Table 2 parameters has 4 current steps, but in practice fewer are often observed due to simulation stop conditions. The color-coded examples are labeled with numbers 1-4 for clarity, establishing connection between panels a-d.

of the joint profiles, and the Supplementary Information details the careful design of the protocol generation algorithm.

The computed cell voltage and irreversible Li plating for four unique charging conditions is highlighted in Figs. 4c-d. Examples 1 and 3 show how irreversible Li plating typically increases exponentially with time (or State of Charge) under constant current charging conditions as in Fig. 1. Example 2, however, interestingly shows that Li plating may start and then subside in response to increasing temperature while at fixed current (Figs. 4a-c #2). Another effect of the notable temperature ramp is that the voltage is observed to decrease with increasing state of charge (Fig. 4d #2). Example 4 similarly shows that irreversible Li plating can be abruptly stopped in response to a current decrease (Fig. 4a,c #4). The stars denote the point at which irreversible Li plating exceeds the threshold we define as the plating onset.

Of the 1000 fast-charging conditions attempted, 600 induced notable Li plating, summarized in Figs. 5a-d. The visualization confirms that Li plating was studied over a comprehensive range of currents, temperatures, and SOC. Fig. 5e plots the plating onsets, which are the end points of the voltage curves in Fig. 5d. The plating onsets are tightly clustered despite the wide range of experimental conditions. It is expected that the plating onset voltages generally increase with increasing SOC, following the cell open-circuit voltage dependence on SOC. The red oval

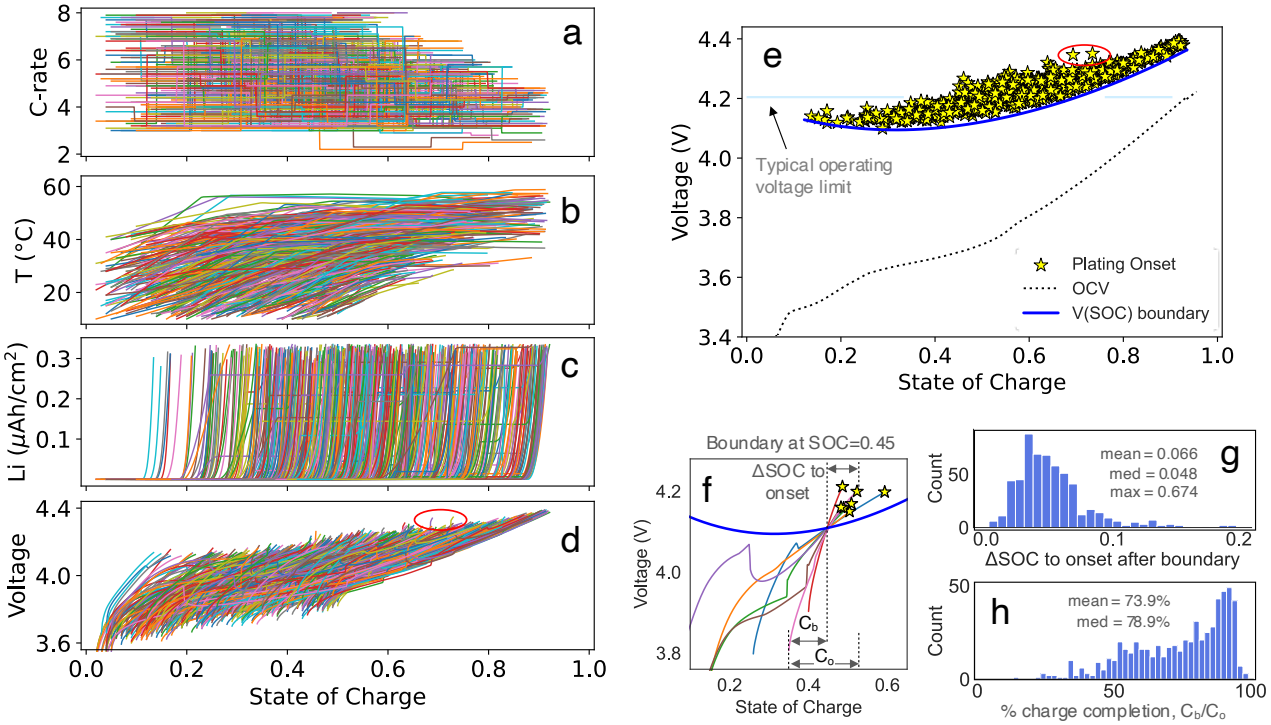

Fig. 5 | Meta-analysis of Li plating onset conditions for diverse fast charging protocols. a-b, Model inputs, and **c-d,** model outputs for n=600 simulations, as in Fig. 4, that induce irreversible Li plating above the onset threshold. **e,** Plating onsets for all simulations, which correspond to the charging voltage curve endpoints in (d). The boundary is an empirical curve sketched along the lowest stars in the cluster, indicating a possible operating voltage constraint to avoid plating. The red ovals in (d) and (e) emphasize the connection between the plots. **f,** Shows charging curves from (d) that intersect the plating boundary at 0.45 ± 0.003 SOC. **g,** Distribution of the capacity remaining after the boundary, before the plating onset (ΔSOC to onset). This equals (C_o - C_b), the onset capacity minus the boundary capacity. The large values (max=0.674) result from either a notable current drop or temperature rise after the boundary is exceeded. **h,** Distribution of the percent charge completion attained by the time the voltage hits the boundary, where full completion (100%) means the charge stops exactly at the plating onset. This equals C_b/C_o from (f).

highlights two points that are separate from the clustering, and the corresponding voltage profiles in Fig. 5d indicate that the current was abruptly increased prior to the start of Li plating, explaining the jump in the cell voltage.

An exciting empirical result from this meta-analysis is that there is a minimum voltage below which plating does not occur, dependent on present SOC (Fig. 5e, blue curve). This boundary curve could inform when to conservatively stop fast-charging or, better, when to calculate the next optimal step in a charge sequence. Fig. 5f illustrates, however, that voltage curves crossing the boundary at the same SOC can have variable plating onsets. To quantify the conservatism of the universal boundary curve approach, we first plot the charge capacity remaining after the boundary until the onset of plating (ΔSOC to onset, Figs. 5f-g). This shows that the plating onset typically occurs within 0.05 SOC after reaching the boundary. Next, we quantify the fractional charge completion achieved up to the boundary relative to the total charge capacity before Li plating (C_b/C_o, Figs. 5f,h). This highlights that, on average, about 75% of the maximum safe charge capacity is attained. Overall, this very simple battery operating constraint could prove useful and complementary to other controls methods, including those that map safe current rates as a function of the operating voltage[23], SOC[25], or estimated graphite critical surface concentration[24] using reduced-order electrochemical models.

Plating prevention with battery aging

In culmination, we add the aging effects (Table 1) to the diverse fast-charging conditions (Table 2) to understand how the plating voltage boundary may vary with age. To simulate a variety of possible aging impacts without presupposing specific aging mechanisms, parameter values are drawn from health-dependent distributions (Fig. 6a). We represent the extent of degradation to each aging parameter as a health index, which ranges from 1 at beginning-of-life to 0.8 at end-of-life. This is analogous to state-of-health, but we refrain from using the term because it is often synonymous with remaining battery capacity. For example, minimally aged cells with health index of 0.98 draw aging parameters that are only slightly worse than their initial values with relatively tight distribution; parameters for extensively aged cells, in contrast, may be much worse than their initial values and vary substantially across draws, reflecting the increasing variability of cell performance with aging due to variability of cell failure mechanisms, operating heterogeneity, and manufacturing defects.

Figs. 6b-e show Li plating onsets from 500 simulations at health indices of 0.98, 0.95, 0.9, and 0.85, which can be be compared to the beginning-of-life results in Fig. 5e. Unsurprisingly, the Li plating onset becomes more variable for the lower health indices due to increased aging parameter variability, making it necessary to adjust the voltage plating boundary strategy in accordance to cell health. This result is also a useful demonstration of why Li plating can occur unexpectedly in aged cells despite using voltage cutoffs that are well below Li plating thresholds at beginning-of-life. In Fig. 6f, we overlay the plating voltage boundaries required to maintain safe charging at each health index. Because the variable-health boundaries are adjusted to the worst-performing cells, it is expected that the voltage boundary approach becomes more conservative with aging. Interestingly, Fig. 6g shows that the plating onset still typically occurs about 0.05 SOC after the boundary regardless of the health index, as in the beginning-of-life cells (Fig. 5g). The mean percent charge acceptance up to the boundary, in contrast, declines notably from 72% to 58% as

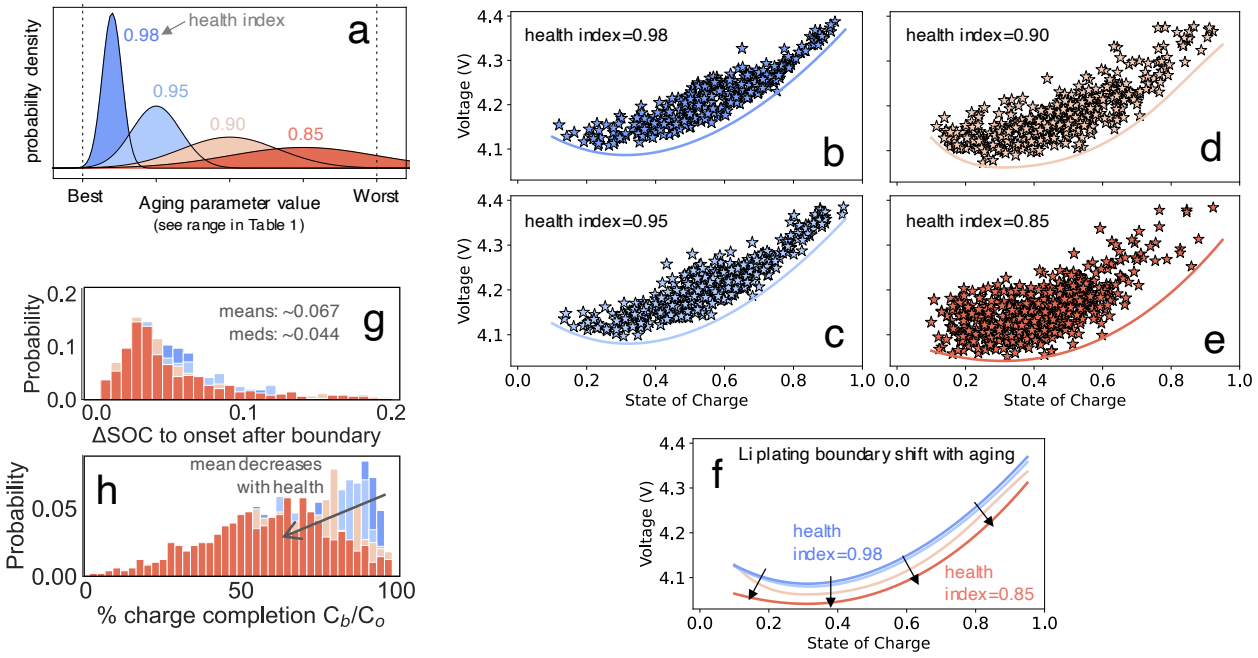

Fig. 6 | The effect of aging on Li plating onsets and operating voltage boundaries. a, The distributions from which aging parameters were selected for battery pack health indices ranging 0.98→0.85, where health index=1 means the Best value and health index=0.8 means the Worst value of Table 1. For a simulation at a specified health, each parameter is drawn independently from the specified distribution, resulting in moderate correlation of aging parameters based on the health, with larger variability for lower-health packs. **b-e,** Li plating onsets for multistep fast charging protocols with correlated aging. 500 conditions were tested for each health index, and the number of simulations inducing Li plating were n=330, n=408, n=443, and n=484 (plotted) for health indices 0.98→0.85 respectively. **f,** Overlay of operating voltage boundaries from data in (b-e). **g-h,** Overlaid distributions of (g) the capacity remaining after the boundary, before the plating onset (ΔSOC to onset) and (h) the percent charge completion attained by the time the voltage hits the boundary, for each health index using the curves in (f).

the health index is lowered from 0.98 to 0.85 (Fig. 6h). The value of an accurate plating model thus increases as cell health degrades. The demonstrated aging analysis may also provide insight for fast-charging battery warranty development.

Finally, we explore whether the plating onset proximity to the boundary relates to certain charging conditions. Without aging, simulations with onset voltages near the boundary tend to have lower initial SOC, access broader SOC windows (compare Fig. S4b,g,l), and exhibit higher charging temperatures (compare Fig. S4c,h,m). With aging, onset voltages are lowered to the greatest extent when the anode parameters (exchange current, voids) are worse than expected and cathode parameters (loss of active material, voids) are better than expected (Fig. S7 and Table S1). These relative changes mimic an effective decrease in the cell negative-to-positive capacity ratio (N/P). Our previous sensitivity analysis explains that the anode effects notably shift the plating onset SOC, and thus voltage, to lower values (Fig. 2e,g), while the limited cathode aging maintains low cell voltage (Fig. 2f,l).

Conclusion and Outlook

This work importantly shows that cell voltage differences correlate with differences in plating onset SOC and that a lower voltage boundary may prevent Li plating across variable operating conditions. There are many opportunities to expand upon the demonstrated approach and findings. Validated P2D models could be further applied to develop optimal charge protocols, such as where

the graphite potential is fixed at the Li plating limit, at diverse imposed temperatures and SOC. A similar workflow may be used for cathode materials such as lithium iron phosphate (LFP) that have unique voltage profiles and may differently affect fast charge capability[38]. In particular, the flat voltage profile of LFP or other phase-transformation positive electrode materials may cause the voltage-boundary approach demonstrated here to be excessively conservative. 3D modeling will be necessary to consider effects of heterogeneous aging or temperature distribution in large-format cells; 18650 cell internal temperature gradients may be minimal (< 5ºC) without active thermal management[39], the scenario where our results are most transferrable, but can reach 20ºC difference with pulse charging and external cooling[40]. Finally, experimental cell aging studies can be combined with in-situ Li plating quantification[31] to further refine this approach and elucidate modifications needed for real-world application.

Overall, we demonstrate combined modeling and data-driven approaches to connect measurable voltage values to difficult-to-predict phenomena such as Li plating. The emphasis on understanding the underlying mechanisms will enable reliable machine learning models that use the voltage and other inputs to predict Li plating for diverse conditions.

References

1. Kempton, W. Electric vehicles: Driving range. *Nat. Energy* **1**, (2016).

2. Arora, P., Doyle, M. & White, R. E. Mathematical Modeling of the Lithium Deposition Overcharge Reaction in Lithium-Ion Batteries Using Carbon-Based Negative Electrodes. *J. Electrochem. Soc.* **146**, 3543 (1999).

3. Tang, M., Albertus, P. & Newman, J. Two-Dimensional Modeling of Lithium Deposition during Cell Charging. *J. Electrochem. Soc.* **156**, A390 (2009).

4. Cannarella, J. & Arnold, C. B. The Effects of Defects on Localized Plating in Lithium-Ion Batteries. *J. Electrochem. Soc.* **162**, A1365–A1373 (2015).

5. Colclasure, A. M. *et al.* Requirements for Enabling Extreme Fast Charging of High Energy Density Li-Ion Cells while Avoiding Lithium Plating. *J. Electrochem. Soc.* **166**, A1412–A1424 (2019).

6. Attia, P. M. *et al.* Review—"Knees" in Lithium-Ion Battery Aging Trajectories. *J. Electrochem. Soc.* (2022) doi:10.1149/1945-7111/ac6d13.

7. Zhang, S. S., Xu, K. & Jow, T. R. Study of the charging process of a LiCoO2-based Li-ion battery. *J. Power Sources* **160**, 1349–1354 (2006).

8. Yang, X. G., Leng, Y., Zhang, G., Ge, S. & Wang, C. Y. Modeling of lithium plating induced aging of lithium-ion batteries: Transition from linear to nonlinear aging. *J. Power Sources* **360**, 28–40 (2017).

9. Rao Koleti, U., Quang Dinh, T. & Marco, J. A new on-line method for lithium plating detection in lithium-ion batteries. *J. Power Sources* **451**, 227798 (2020).

10. Smith, A. J. *et al.* Localized lithium plating under mild cycling conditions in high-energy lithium-ion batteries. *J. Power Sources* **573**, (2023).

11. Dufek, E. J. *et al.* Developing extreme fast charge battery protocols – A review spanning materials to systems. *J. Power Sources* **526**, 231129 (2022).

12. Tomaszewska, A. *et al.* Lithium-ion battery fast charging: A review. *eTransportation* **1**, 100011 (2019).

13. Mai, W., Colclasure, A. M. & Smith, K. Model-Instructed Design of Novel Charging Protocols for the Extreme Fast Charging of Lithium-Ion Batteries Without Lithium Plating. *J. Electrochem. Soc.* **167**, 080517 (2020).

14. Sieg, J. *et al.* Fast charging of an electric vehicle lithium-ion battery at the limit of the lithium deposition process. *J. Power Sources* **427**, 260–270 (2019).

15. Waldmann, T., Kasper, M. & Wohlfahrt-mehrens, M. Optimization of Charging Strategy by Prevention of Lithium Deposition on Anodes in high-energy Lithium-ion Batteries –

Electrochemical Experiments. *Electrochim. Acta* **178**, 525–532 (2015).

16. Epding, B., Rumberg, B., Mense, M., Jahnke, H. & Kwade, A. Aging-Optimized Fast Charging of Lithium Ion Cells Based on Three-Electrode Cell Measurements. *Energy Technol.* **8**, 1–9 (2020).

17. Jiang, B. *et al.* Bayesian learning for rapid prediction of lithium-ion battery-cycling protocols. *Joule* **5**, 3187–3203 (2021).

18. Attia, P. M. *et al.* Closed-loop optimization of fast-charging protocols for batteries with machine learning. *Nature* **578**, 397–402 (2020).

19. Klein, R. *et al.* Optimal charging strategies in lithium-ion battery. *Proc. Am. Control Conf.* 382–387 (2011) doi:10.1109/acc.2011.5991497.

20. Perez, H., Shahmohammadhamedani, N. & Moura, S. Enhanced Performance of Li-Ion Batteries via Modified Reference Governors and Electrochemical Models. *IEEE/ASME Trans. Mechatronics* **20**, 1511–1520 (2015).

21. Romagnoli, R., Couto, L. D., Goldar, A., Kinnaert, M. & Garone, E. A feedback charge strategy for Li-ion battery cells based on Reference Governor. *J. Process Control* **83**, 164–176 (2019).

22. Hahn, M. *et al.* Model predictive fast charging control by means of a real-time discrete electrochemical model. *J. Energy Storage* **42**, 103056 (2021).

23. Couto, L. D. *et al.* Faster and Healthier Charging of Lithium-Ion Batteries via Constrained Feedback Control. *IEEE Trans. Control Syst. Technol.* **30**, 1990–2001 (2022).

24. Drummond, R., Courtier, N. E., Howey, D. A., Couto, L. D. & Guiver, C. Constrained optimal control of monotone systems with applications to battery fast-charging. 1–13 (2023).

25. Wassiliadis, N., Kriegler, J., Abo, K. & Lienkamp, M. Model-based health-aware fast charging to mitigate the risk of lithium plating and prolong the cycle life of lithium-ion batteries in electric vehicles. *J. Power Sources* **561**, 232586 (2023).

26. Liu, T., Ge, S., Yang, X. G. & Wang, C. Y. Effect of thermal environments on fast charging Li-ion batteries. *J. Power Sources* **511**, 230466 (2021).

27. Keyser, M. *et al.* Enabling fast charging – Battery thermal considerations. *J. Power Sources* **367**, 228–236 (2017).

28. Zeng, Y. *et al.* Extreme fast charging of commercial Li-ion batteries via combined thermal switching and self-heating approaches. *Nat. Commun.* 1–9 (2023) doi:10.1038/s41467-023-38823-9.

29. Tanim, T. R., Shirk, M. G., Bewley, R. L., Dufek, E. J. & Liaw, B. Y. Fast charge implications: Pack and cell analysis and comparison. *J. Power Sources* **381**, 56–65 (2018).

30. Zilberman, I., Ludwig, S., Schiller, M. & Jossen, A. Online aging determination in lithium-ion battery module with forced temperature gradient. *J. Energy Storage* **28**, 101170 (2020).

31. Konz, Z. M. *et al.* High-throughput Li plating quantification for fast-charging battery design. *Nat. Energy* (2023) doi:10.1038/s41560-023-01194-y.

32. Colclasure, A. M. *et al.* Electrode scale and electrolyte transport effects on extreme fast charging of lithium-ion cells. *Electrochim. Acta* **337**, 135854 (2020).

33. McShane, E. J. *et al.* Quantification of Inactive Lithium and Solid–Electrolyte Interphase Species on Graphite Electrodes after Fast Charging. *ACS Energy Lett.* **5**, 2045–2051 (2020).

34. Smith, R. B., Khoo, E. & Bazant, M. Z. Intercalation Kinetics in Multiphase-Layered Materials. *J. Phys. Chem. C* **121**, 12505–12523 (2017).

35. Chen, Z. *et al.* Overpotential analysis of graphite-based Li-ion batteries seen from a porous electrode modeling perspective. *J. Power Sources* **509**, 230345 (2021).

36. Weddle, P. J. *et al.* Battery State-of-Health Diagnostics During Fast Cycling Using Physics-Informed Deep-Learning. (2023).

37. Pegel, H. *et al.* Fast-charging performance and optimal thermal management of large-format full-tab cylindrical lithium-ion cells under varying environmental conditions. *J. Power Sources* **556**, 232408 (2023).

38. Adam, A., Wandt, J., Knobbe, E., Bauer, G. & Kwade, A. Fast-Charging of Automotive Lithium-Ion Cells: In-Situ Lithium-Plating Detection and Comparison of Different Cell Designs. *J. Electrochem. Soc.* **167**, 130503 (2020).

39. T. Heenan. Mapping internal temperatures during high-rate battery applications. *Nature* **617**, (2023).

40. Fleckenstein, M., Bohlen, O., Roscher, M. A. & Bäker, B. Current density and state of charge inhomogeneities in Li-ion battery cells with LiFePO4 as cathode material due to temperature gradients. *J. Power Sources* **196**, 4769–4778 (2011).

41. Christensen, J. & Newman, J. Cyclable Lithium and Capacity Loss in Li-Ion Cells. *J. Electrochem. Soc.* **152**, A818–A829 (2005).

42. Kim, Y., Seong, W. M. & Manthiram, A. Cobalt-free, high-nickel layered oxide cathodes for lithium-ion batteries: Progress, challenges, and perspectives. *Energy Storage Mater.* **34**, 250–259 (2021).

43. Ho, A. S. *et al.* 3D Detection of Lithiation and Lithium Plating in Graphite Anodes during Fast Charging. *ACS Nano* **15**, 10480–10487 (2021).

44. Petz, D. *et al.* Aging-Driven Composition and Distribution Changes of Electrolyte and

Graphite Anode in 18650-Type Li-Ion Batteries. *Adv. Energy Mater.* **12**, (2022).

45. Thompson, L. M. *et al.* Quantifying Changes to the Electrolyte and Negative Electrode in Aged NMC532/Graphite Lithium-Ion Cells. *J. Electrochem. Soc.* **165**, A2732–A2740 (2018).

Supplementary Information

COMSOL Simulations. The pseudo-2D model based on the Doyle-Fuller-Newman framework was simulated with COMSOL software using the Lithium-ion Battery module. Model parameter values and equations have been extensively justified in previous works[5,31–33,36], some of which are reproduced below. Here we highlight important notes or differences from past studies. First, for Fig. 1 simulations performed to compare with past experiments, the initial temperature was specified to be 30 ºC but the simulation is not isothermal. The computed temperature rise based on previously validated thermal properties was 2.4, 3.9, and 6.5 ºC for the rates of 3.75C, 5C, and 7.5C respectively. For all other simulations, the temperatures were user-defined; the Fig. 2 sensitivity analysis was performed isothermally and the multi-step protocols used piecewise temperature functions. In COMSOL, the user-defined temperature was achieved with a Heat Flux component within the Heat Transfer in Solids module. At both electrode current collectors, the convective heat flux was applied as

$$q_0 = h \cdot (T_{ext} - T)$$

where T_{ext} is the external temperature defined by the piecewise function, T is the cell temperature at the boundary, and h is the convection heat transfer coefficient. To force the cell temperature to rapidly approach T_{ext}, h is multiplied by 10^3 to give 6000 W/m^2·K.

For the piecewise functions used for the multistep protocol, the current inputs are four C-rate values corresponding to the unique time steps. The SOC interval corresponding to each current step is split into 2 for a total of 8 temperature steps. The temperature piecewise function is defined by 8 step end-time parameters (s), 8 start-temperature values (ºC), and 8 temperature ramp values (ºC/s). Writing the piecewise function in terms of model-defined parameters enabled use of the Parametric Study option to systematically vary those parameters and quickly simulate thousands of different conditions. Simulation stop criteria were added to prevent simulations from exceeding 4.4V or 0.1% irreversible Li plating, the regions of interest for this study. While 0.01% irreversible Li plating was used to define the plating onset threshold, Fig. S6 shows that changing this value has a small effect on the analysis herein. Data analysis and visualization was performed in Python using a combination of the Pandas, SciPy, Seaborn, and matplotlib libraries.

Aging mechanism and parameter value selection. The aging mechanisms were selected to be representative of commonly reported battery failure modes. Loss of active material and loss of lithium inventory have been long reported and studied[41]. Up to 20% loss of active material for the cathode was considered, higher than 10% for the anode, because cathodes are continually innovated to less-stable higher-nickel content NMC[42] or LFP-based chemistries based on supply chain, whereas graphite has been continually optimized over decades. Gas-producing interfacial reactions are possible at the low-voltage anode and high-voltage cathode, so void formation within the electrode pores was considered due to possible gas displacement of electrolyte. Similarly, electrode expansion is considered due to the common macroscopic observation of battery swelling. The maximum expansion value of ~10% was selected from knowledge that the battery casing constrains the expansion, and that graphite can expand up to 10% in the fully lithiated state[43]. Another universal aging mechanism is the electrode-electrolyte interface (SEI) growth or

composition change throughout cycling, one contributor to increased cell polarization with cycling. We opted to represent these phenomena by modifying the exchange current density at each electrode, worsening the reaction kinetics and increasing resistance to charge transfer. We did this for simplicity, rather than attempting to add new resistance elements which could be considered in future works. Finally, we considered ionic conductivity changes to reflect the possibility of electrolyte composition changes throughout cycling. Other electrolyte property changes such as changing concentration of Li-ion conducting salts[44] could be considered, but we focused on the above more widely-reported mechanisms due to some evidence that electrolyte may not change significantly with aging[45], and noting that this phenomena varies significantly by chemistry.

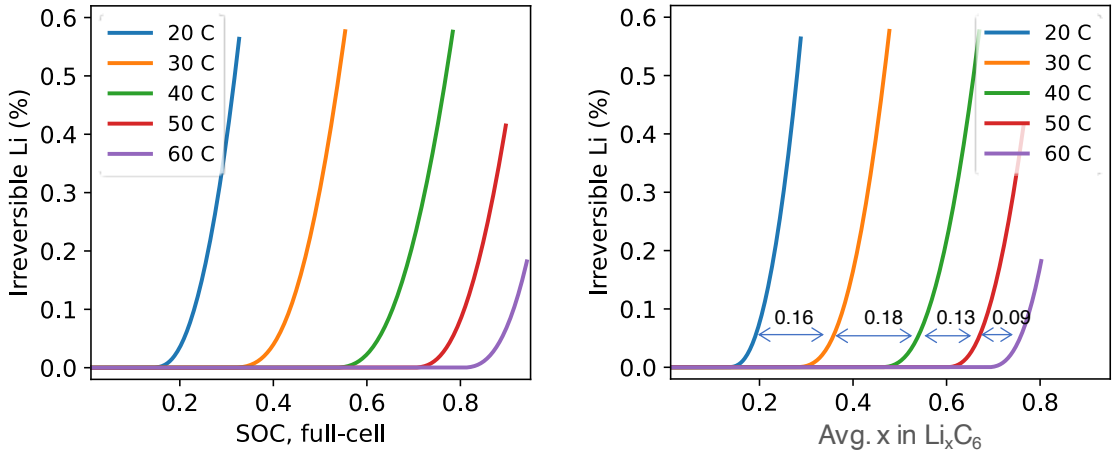

Fig. S1. Calibrated model response to initial temperature change, 6C rate. This illustrates that the Gr|NMC532 model temperature response to Li plating is reasonable given past half-cells Li plating temperature studies of Ref. [31], which estimate a plating onset change (x-direction shift of curves) of about 0.01 Graphite SOC per 1ºC. The data in the right plot are the same as the left, except the x-axis is recast as the expected average graphite electrode lithiation, to enable comparison with past half-cells. The shifts with 10ºC temperature change range 0.09-0.18 SOC.

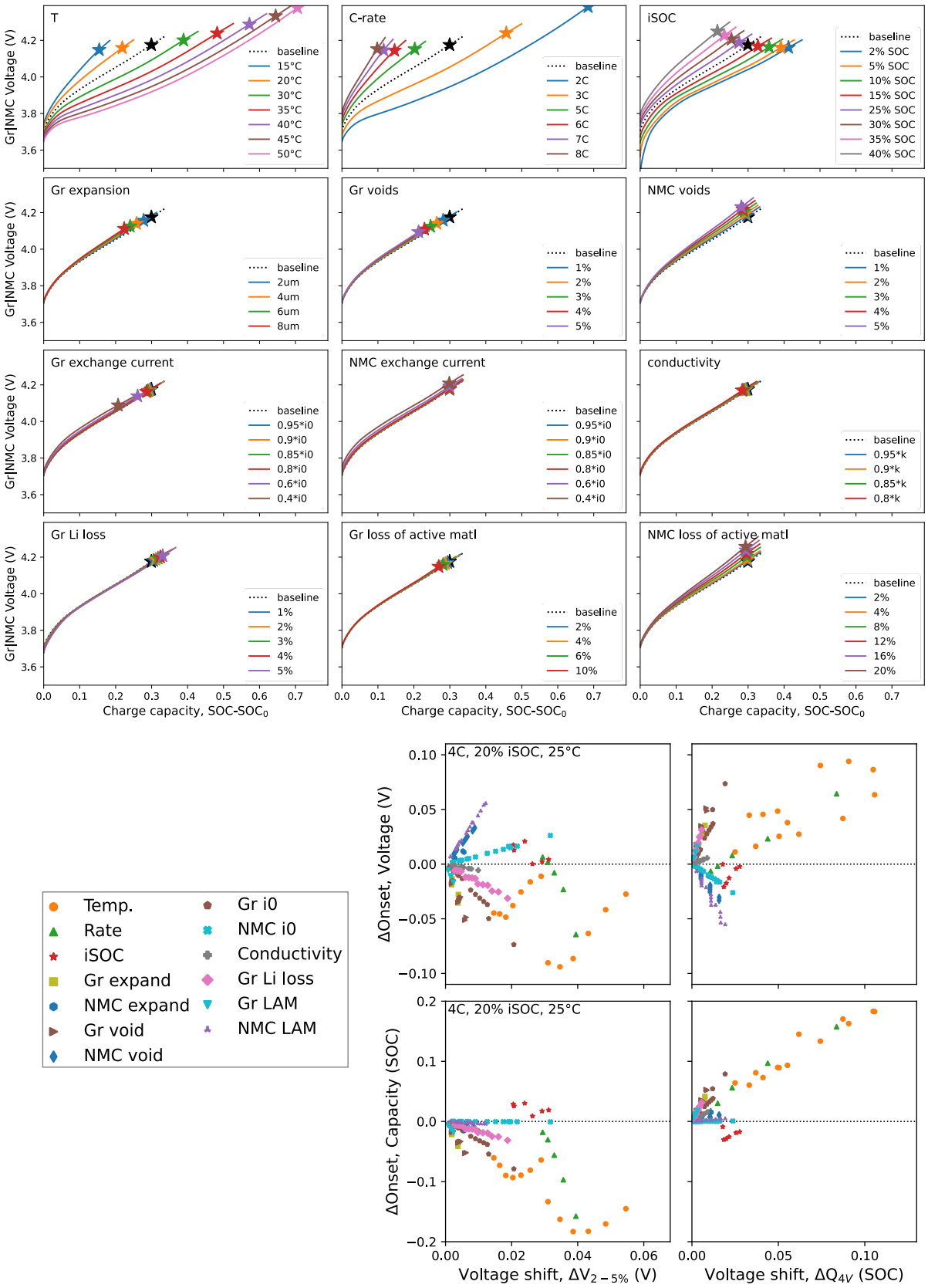

Fig. S2. Sensitivity analysis of Fig. 2Fig. 3 performed with baseline charging conditions of 4C, 25°C, 20% initial SOC, and no aging. Trends are similar despite different temperature, SOC, and rate.

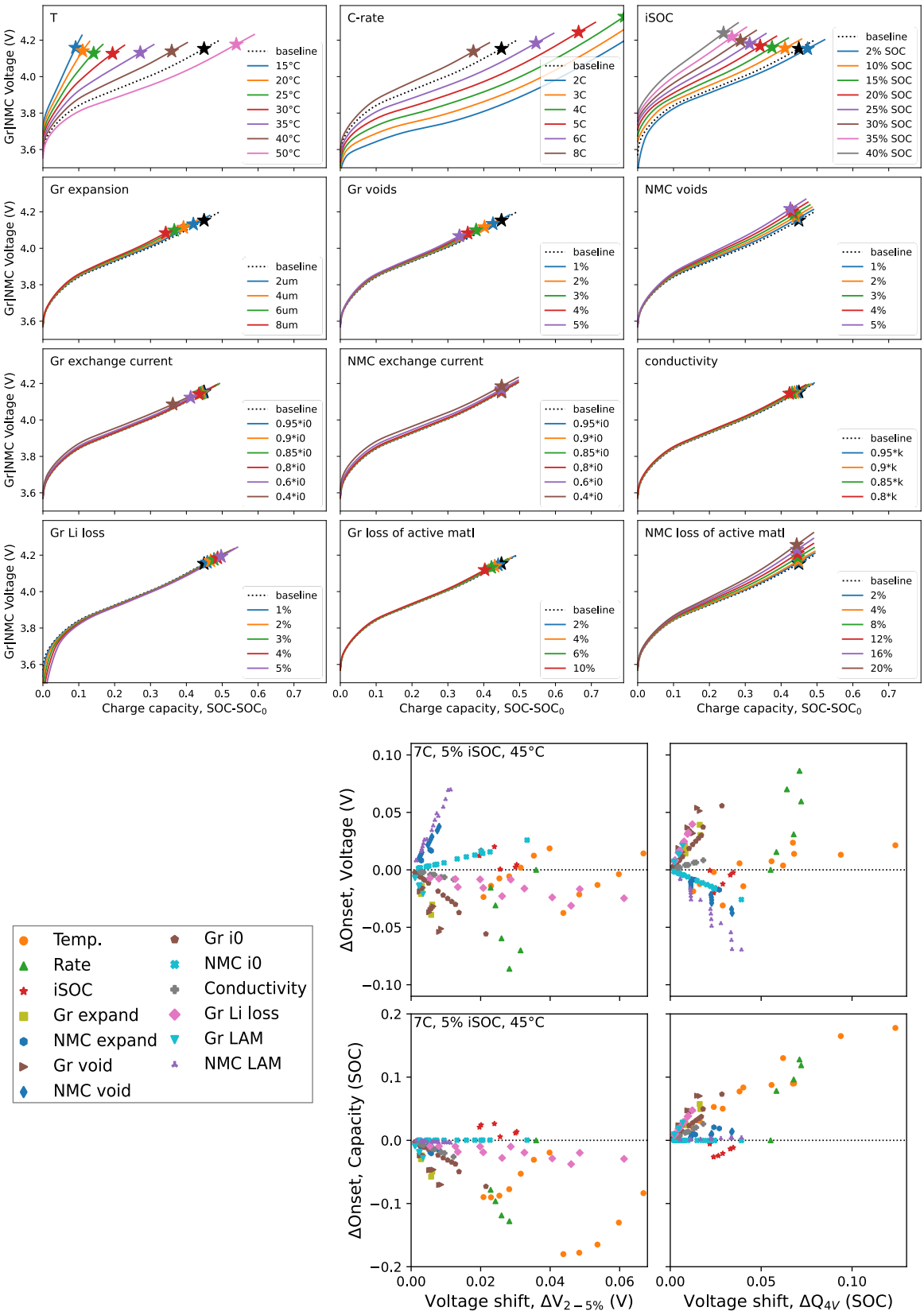

Fig. S3. Sensitivity analysis of Fig. 2Fig. 3 performed with baseline charging conditions of 7C, 45°C, 5% initial SOC, and no aging. Trends are similar despite different temperature, SOC, and rate.

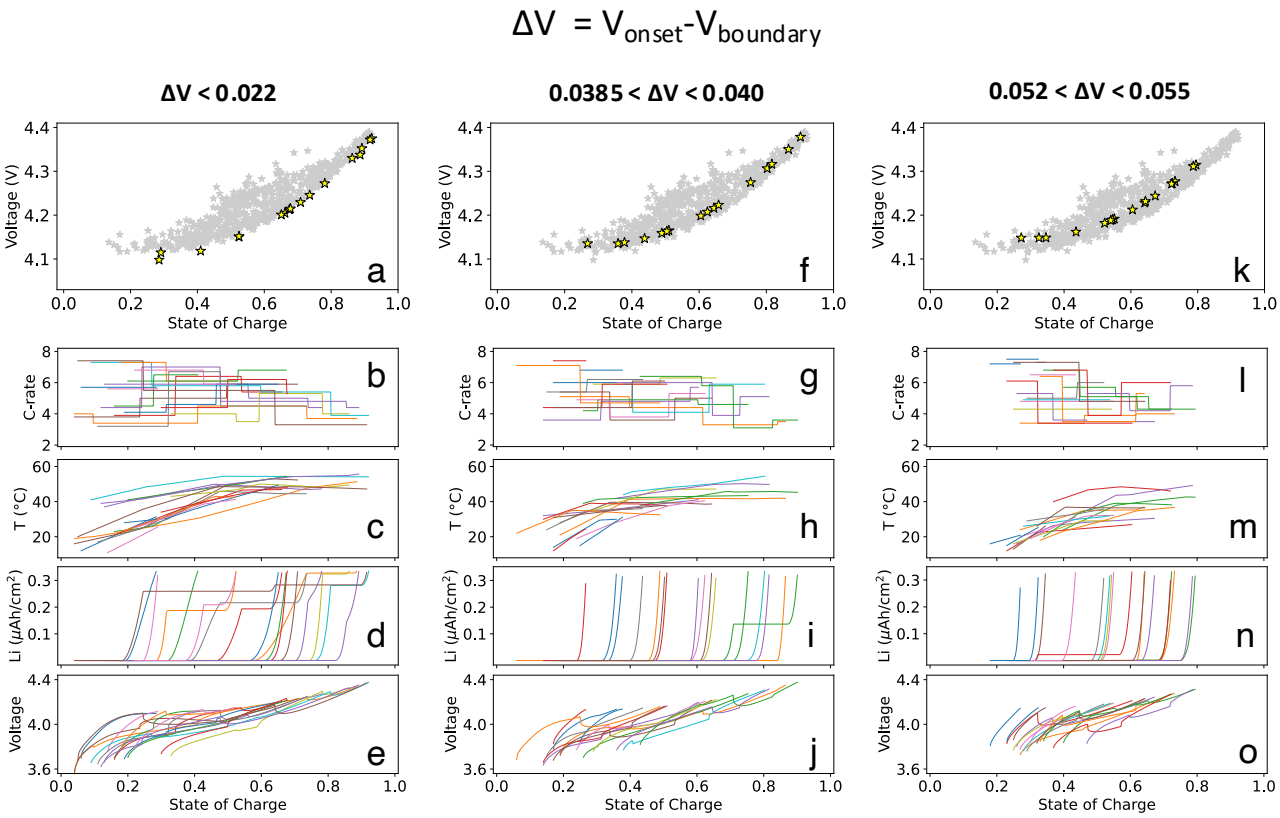

Fig. S4. Understanding the phenomenon of varied plating onset distances from the voltage boundary. We attempted to understand if simulations with plating onsets near or far from the voltage boundary shared any characteristics. The ranges were selected so that similar number of simulations (n~15) are in each set of plots. **a,** Highlights the data points investigated from Fig. 5e that have plating onset voltages within 0 to 0.022 V of the boundary. **b-e,** The rate, temperature, Li plating, and voltage profiles corresponding to (a). **f,** Data points with plating onset voltages between 0.0385 to 0.040 V of the boundary. **g-j,** The rate, temperature, Li plating, and voltage profiles corresponding to (f). **k,** Data points with plating onset voltages between 0.052 to 0.055 V of the boundary. **l-o,** The rate, temperature, Li plating, and voltage profiles corresponding to (k). Discussion: In general, onsets near the boundary access broader SOC windows (compare b,g,l), have lower initial SOC, and exhibit higher charging temperatures (compare c,h,m). Also, many of the low-voltage plating onset conditions exhibit rapid current drops or temperature rises that interrupt Li plating accumulation, shown by the unique curve shapes in (d), causing the onset threshold to be exceeded at later SOC in the same charge.

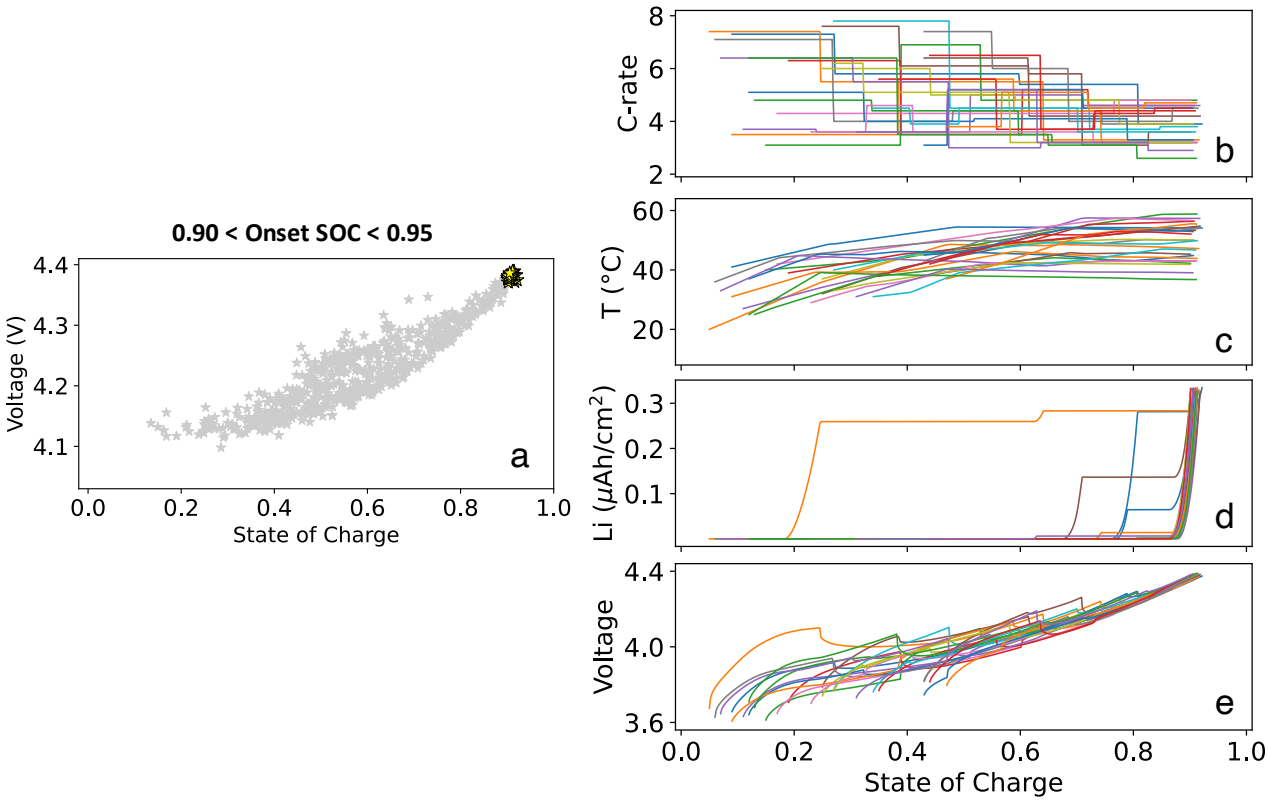

Fig. S5. Understanding the conditions that lead to plating onsets at high SOC. We attempted to understand if simulations with plating onsets at high SOC – an indication that successful fast charging to 80% is possible – possess any interesting shared characteristics. **a,** Highlights the data points investigated from Fig. 5e that have plating onset SOC between 0.90 and 0.95. **b-e,** The rate, temperature, Li plating, and voltage profiles corresponding to (a). **Discussion:** First, (b) and (c) show that successful fast charging can occur at many combinations of temperature and C-rate. Next, by 50% SOC, all cell temperatures are above 38ºC, and by 75% SOC, nearly all rates are below 5C except the single cell that was initially charged to 50ºC (blue curve). Finally, the voltage profiles (e) converge above 0.8 SOC despite variable T, C-rate, and voltage history. This further supports the hypothesis of the main text that the voltage, affected collectively by many phenomena, may correlate well with plating onset.

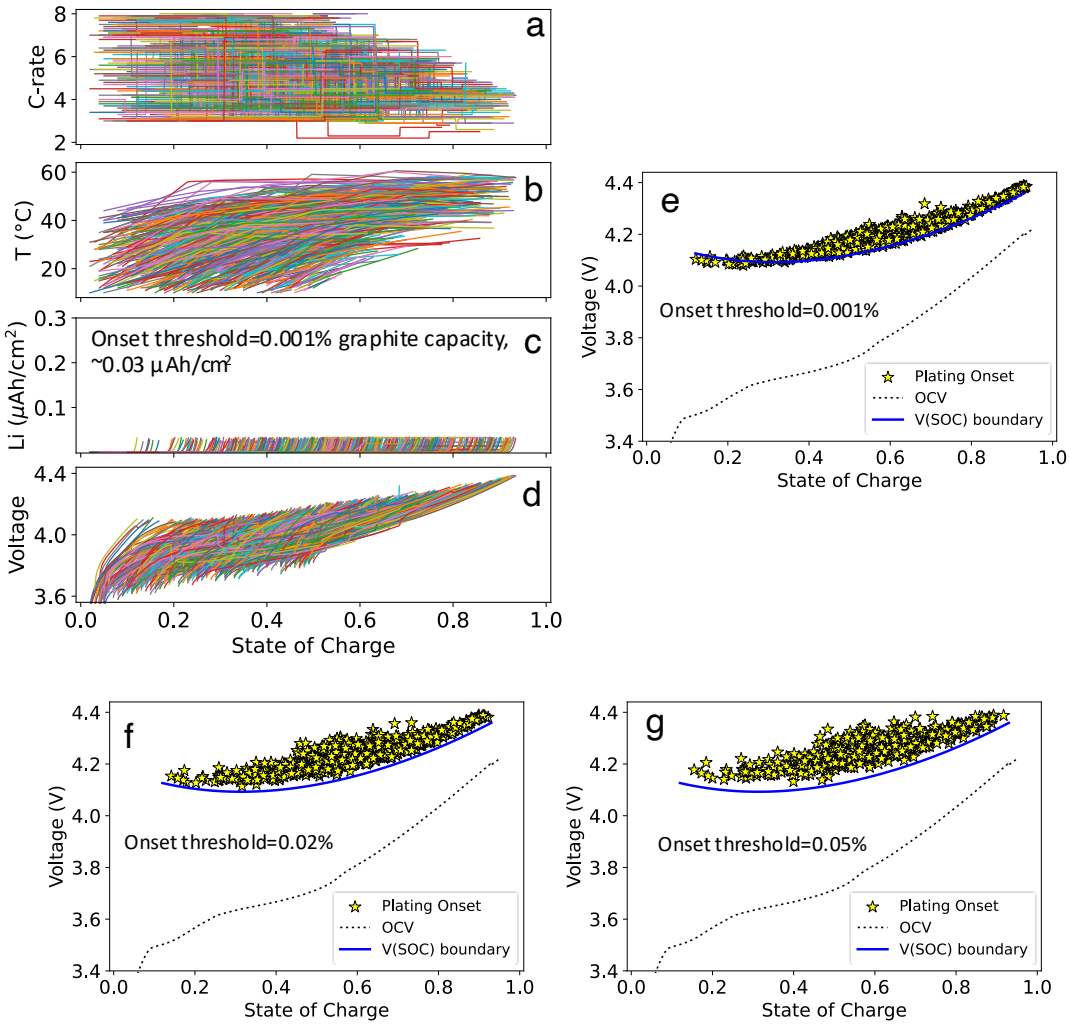

Fig. S6. The effect of changing the user-defined plating onset threshold. a-d, All simulations from the no-aging analysis of Fig. 5 that exceed 0.001% graphite capacity of lithium plating, a lower threshold than 0.01% used throughout the work. The data are plotted until the threshold is exceeded, as evidenced by (c). **e-g,** The plating onset voltages and SOC for thresholds of 0.001%, 0.02%, and 0.05% respectively, overlaid with the voltage boundary derived from the 0.01% threshold used throughout the manuscript. The stars shift slightly down or up relative to the boundary, according to the threshold, as expected. Interestingly, the clustering is tighter for the lower threshold (e). This may be due to eliminating some of the variability caused by the stopping and starting of Li plating seen in Fig. S4d.

Table S1. Average aging parameters for simulations with plating onsets near voltage boundary, health index=0.85

mechanism	Normalized mean value (expected=0.85)	Norm. std	mean	std	best	worst	Normalized 0 to 1
an_expansion_um	0.82	0.04	7.23E-06	1.39E-06	0	8.00E-06	0.10
ca_expansion_um	0.88	0.03	4.88E-06	1.36E-06	0	8.00E-06	0.39
an_void	0.82	0.05	0.046	0.012	0	0.05	0.08
ca_void	0.88	0.07	0.029	0.017	0	0.05	0.41
an_i0_factor	0.79	0.05	0.482	0.121	1	0.5	-0.04
ca_i0_factor	0.87	0.05	0.682	0.118	1	0.5	0.36
cond_factor	0.87	0.07	0.866	0.070	1	0.8	0.33
an_LiLoss	0.85	0.04	0.059	0.015	0	0.08	0.26
an_LAM	0.85	0.04	0.076	0.018	0	0.1	0.24
ca_LAM	0.9	0.04	0.098	0.039	0	0.2	0.51

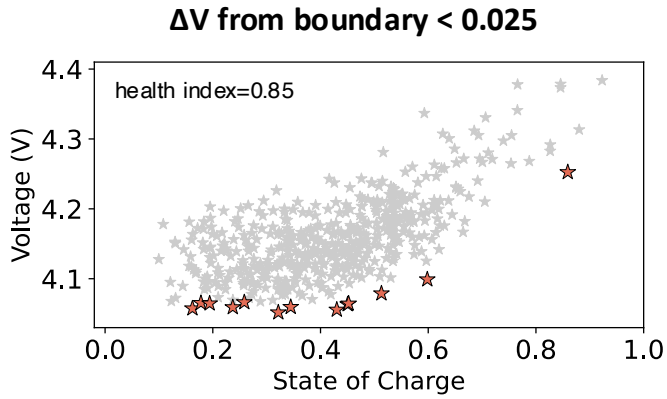

Fig. S7. Data points analyzed near boundary for health index=0.85, used in Table S1. The 13 data points analyzed have plating onset voltages within 0.025 V of the boundary in Fig. 6e.

Charge protocol generation algorithm. In this description, variables are selected randomly from a uniform (flat) distribution unless specified. **1) Random starting variable selection.** Random current values are selected for steps 1-3 between the [Min, Max] values provided in Table 2, then the current for step 4 is randomly selected such that it cannot be 0.5C larger than step 3. This constraint was added because it is unrealistic for a large current increase near the end of charge. An initial SOC is randomly selected, and then the ΔSOC for each of the 8 temperature steps are randomly generated so that the proposed charge would reach the target Stop SOC of 0.95. The initial charging temperature is randomly selected and then the charging target temperature, which must be at least 5 ºC higher than initial, is selected. This constraint maintains that batteries will heat some, naturally occurring and desirable for avoiding Li plating, during fast charge. **2) Calculate the first step of the piecewise temperature function.** Based on the initial rate and temperature, a semi-random initial temperature ramp is selected. The initial temperature is normalized between 0 and 1 according to the minimum and maximum initial values. A random value x is drawn from the normal distribution with μ=(1-$T_{i,norm}$) and σ=0.4 is selected and constrained to 0 < x < 1. Then this value is scaled according to the minimum (0) and maximum (1) temperature ramp rates (m) expected for the given rate *I*, with ramp rates given by:

$$m_{min}(°C/s) = \frac{I^2}{I_{ref}^2}\, m_{ref,min}$$

$$m_{max}(°C/s) = \frac{I^2}{I_{ref}^2}\, m_{ref,max}$$

This was done to incorporate the logic that for lower initial temperatures, higher temperature ramps are likely desired to achieve high-temperature conditions most suitable for fast-charging. This also captures the idea that temperature ramp values should be higher for higher C-rates, roughly scaling with an I^2 dependence derived from joule heating (I^2R) of an electrical conductor. **3) Calculate remaining steps of the piecewise temperature function.** For each remaining step, ramp rates are calculated according to the historical temperature. If the target temperature has been exceeded, then the temperature ramp will fluctuate randomly within a range of values, positive or negative, to capture uneven heating or cooling effects. The temperature drift factor of Table 2, 0.2, is multiplied by the m_{max} to constrain the fluctuation ramp values, which vary with C-rate. If the target temperature has not been reached, then either i) If the C-rate of the next step is the same, then the temperature ramp is kept approximately the same with some added noise to account for real-life variability or curvature, or ii) If the C-rate of the next step is different than the previous, a new semi-random temperature ramp is selected according to the present temperature and rate according to the function from Section (2). Finally, for all cases, if the proposed temperature ramp for a given step causes the temperature to greatly exceed the target temperature (which might occur if the random ΔSOC for a step is very large), then the ramp is adjusted with knowledge of the future target.

Equation formulation for aging conditions and lithium plating

Electrode expansion, void formation, and loss of active material. The length of the electrode, l ,is increased from its beginning-of-life (BOL) length, l_{BOL}, by $\boldsymbol{l_{expansion}}$. The BOL length is used to calculate electrode capacity from the volume of active material, so other battery operating parameters remain unaffected when expansion is added to the model. The nominal battery properties without added aging have the subscript BOL. The same formulation is used for both electrodes, graphite and NMC532.

$$l = l_{BOL} + \boldsymbol{l_{expansion}}$$

When the electrode thickness is increased, a void fraction is created, and the effect is a decreasing volume fraction of other components (solids, electrolyte, pre-existing voids). This material conservation is captured by multiplying each component fraction by the following expansion factor, which is always ≤ 1 because we only consider positive values for $\boldsymbol{l_{expansion}}$:

$$\left(\frac{l_{BOL}}{l}\right)$$

The equations below relate the solids volume fraction, ε_{solids}, to the BOL value according to the above factor:

$$\varepsilon_{solids,BOL} = 1 - \varepsilon_{elyte,BOL}$$

$$\varepsilon_{solids} = \varepsilon_{solids,BOL}\left(\frac{l_{BOL}}{l}\right)$$

A similar correction is made for the electrolyte fraction ε_{elyte}. Note that the electrolyte fraction can also be affected by direct void formation, a separate mechanism to simulate electrolyte drying or gas formation within electrode pores. We assume this void volume fraction, $\varepsilon_{void,elyte,BOL}$, is present at BOL, prior to electrode expansion, for simplicity:

$$\varepsilon_{elyte} = (\varepsilon_{elyte,BOL} - \boldsymbol{\varepsilon_{void,elyte,BOL}})\left(\frac{l_{BOL}}{l}\right)$$

The fractional loss of active material, $\%\boldsymbol{LAM}$, another aging mechanism, is added to the equation below where ε_{AM} is the volume fraction of active material and CBD_AM is the volume fraction of solids that are non-active carbon binder material:

$$\varepsilon_{AM,anode} = \varepsilon_{solids,anode}(1 - CBD\_AM)(1 - \%\boldsymbol{LAM})$$

Finally, to ensure consistency of the formulation, we confirm in the model that the sum of all volume fractions (electrolyte, active material, carbon binder material, inactive material, expansion-induced voids, electrolyte loss voids – in order, below) equals to 1, regardless of the aging parameter values:

$$\varepsilon_{elyte} + \varepsilon_{AM} + \varepsilon_{AM}\left(\frac{CBD\_AM}{1-CBD\_AM}\right) + \varepsilon_{AM}\left(\frac{\%LAM}{1-\%LAM}\right) + \frac{l_{expansion}}{l} + \varepsilon_{void,elyte,BOL}\left(\frac{l_{BOL}}{l}\right) = 1$$

Charge transfer kinetics decrease and electrolyte conductivity decrease. The exchange current density i_0 [A m^{-2}] for either graphite intercalation or NMC532 de-insertion, the reactions that dominate during battery charge, is multiplied by a coefficient A (≤ 1), increasing the resistance to charge transfer. This coefficient does not affect the dependence of i_0 on solid Li concentration c_s, electrolyte Li^+ concentration c_e, or temperature T. Similarly, the electrolyte conductivity κ_e is multiplied by a coefficient B (≤ 1).

$$i_{0,\text{aging}} = A \cdot i_0(c_s, c_e, T)$$

$$\kappa_{e,\text{aging}} = B \cdot \kappa_e(c_e, T)$$

Lithium inventory loss, electrode slippage. The initial lithium intercalation fraction in the graphite electrode $x_{Gr,i}$ is determined by the initial state-of-charge (SOC_i) and is calculated using the minimum lithium fraction in the graphite $x_{Gr,min}$, the capacities of both electrodes, C_{Gr} and C_{NMC}, and the maximum graphite intercalation fraction change $\Delta x_{max,Gr}$. The loss of lithium inventory $x_{Li,loss}$, is subtracted from $x_{Gr,i}$:

$$x_{Gr,i} = x_{Gr,min} + SOC_i \cdot \Delta x_{max,Gr} \frac{C_{NMC}}{C_{Gr}} - \boldsymbol{x_{Li,loss}}$$

The electrode capacities are calculated from their respective theoretical volumetric lithium concentrations multiplied by the maximum expected intercalation fraction changes Δx. The initial lithium fraction in the NMC electrode $x_{NMC,i}$ is:

$$x_{NMC,i} = x_{NMC,max} - SOC_i \cdot \Delta x_{max,NMC}$$

The change in $x_{Gr,i}$ shifts the graphite potential range accessed during charge, which is why electrode slippage is used to alternately name this effect. We only consider one direction of slippage resulting from irreversible reactions at the graphite electrode, such as Li plating or SEI formation, but believe future work could consider scenarios where the initial graphite lithiation is higher than expected $(x_{Li,loss} < 0)$.

Lithium plating and stripping reaction formulation. The Li plating and stripping reaction j_{Li} is expressed in the Butler-Volmer formulation as

$$j_{Li} = \frac{i_0}{F}\left[exp\left(\frac{(1-\alpha)F(\Phi_s - \Phi_e - U_{OCP})}{RT}\right) - exp\left(\frac{-\alpha F(\Phi_s - \Phi_e - U_{OCP})}{RT}\right)\right],$$

where i_0 is exchange current density, α is the transfer coefficient for plating, U_{OCP} is the open-circuit potential of the plating reaction (0 vs. Li/Li^+), F is Faraday's constant, R is the universal gas constant, and T is the temperature.

In COMSOL, the lithium plating and stripping equations are implemented by adding a Distributed ODE to the graphite electrode domain with conditional statements. If the local voltage, $(\Phi_s - \Phi_e)$, is less than 0 V vs. Li/Li$^+$, then the lithium plating reaction occurs ($j_{Li} < 0$), forming both reversible and irreversible lithium plating:

$$\frac{\partial n_{Li,irrev.}}{\partial t} = -(1-\beta)\, j_{Li}\, A_s$$

$$\frac{\partial n_{Li,rev.}}{\partial t} = -\beta\, j_{Li}\, A_s$$

where $n_{Li,irrev.}$ and $n_{Li,rev.}$ are the concentrations (mol/m^3) of irreversible and reversible lithium plating respectively, A_s is the anode specific surface area with units 1/m, and β is the plating reversibility factor.

If $(\Phi_s - \Phi_e) > 0$, then no plating will occur and:

$$\frac{\partial n_{Li,irrev.}}{\partial t} = 0$$

If $(\Phi_s - \Phi_e) > 0$ and $n_{Li,rev.} > 0$, then Li stripping ($j_{Li} > 0$) will occur and reversible lithium plating will decrease according to:

$$\frac{\partial n_{Li,rev.}}{\partial t} = -\beta\, j_{Li}\, A_s \frac{n_{Li,rev.}}{n_{Li,rev.} + \gamma}$$

where the term containing γ is added to decrease the stripping amount as $n_{Li,rev.}$ approaches 0.

Finally, if $(\Phi_s - \Phi_e) > 0$ and $n_{Li,rev.} \leq 0$, then Li stripping will not occur and:

$$\frac{\partial n_{Li,rev.}}{\partial t} = 0$$

The parameter values used for the Li plating formulation are: i_0 = 10 A/m^2, α = 0.7, U_{OCP} = 0 V, β = 0.8, and γ =0.01.

Table S2. Constant-value model parameters

Variable	Description	Value	Unit
A	Current-collector area	1.54	cm^2
C_{NMC}	Full-cell capacity (Measured & used for C-rates)	2.80	mAh cm^{-2}
C_{Gr}	Anode theoretical capacity (set to match expt.)	3.35	mAh cm^{-2}
$c_{e,0}$	Initial electrolyte concentration	1.2	kmol m^{-3}
$c_{s,max,an}$	Maximum Li concentration in the anode	30.0	kmol m^{-3}
$c_{s,max,an}$	Maximum Li concentration in the cathode	49.6	kmol m^{-3}
$\Delta x_{max,Gr}$	Maximum intercalation fraction change, graphite anode	0.97	-
$x_{Gr,min}$	Minimum graphite anode intercalation fraction	0.02	-
$\Delta x_{max,NMC}$	Maximum intercalation fraction change, NMC cathode	0.58	-
$x_{NMC,max}$	Maximum NMC cathode intercalation fraction	0.89	-
N/P	Anode capacity vs. cathode capacity	1.16	-
t_{an}	Length/thickness of anode	70	µm
t_{sep}	Length/thickness of separator	25	µm
t_{ca}	Length/thickness of cathode	71	µm
$p_{e,an}$	Bruggeman coefficient of electrolyte in anode	2	-
$p_{e,sep}$	Bruggeman coefficient of electrolyte in separator	1.8	-
$p_{e,ca}$	Bruggeman coefficient of electrolyte in cathode	2	-
$p_{s,an}$	Bruggeman coefficient of solid phase in anode	2	-
$p_{s,ca}$	Bruggeman coefficient of solid phase in cathode	2	-
$R_{s,an}$	Average particle radius in anode	4	µm
$R_{s,ca}$	Average particle radius in cathode	1.8	µm
α	Reaction transfer coefficient, all intercalation reactions	0.5	-
$\epsilon_{el,an}$	Electrolyte volume fraction in anode	0.34	-
$\epsilon_{el,ca}$	Electrolyte volume fraction in cathode	0.354	-
$\epsilon_{el,sep}$	Electrolyte volume fraction in separator	0.55	-
$\epsilon_{s,an}$	Solid-phase active material volume fraction in anode	0.60	-
$\epsilon_{s,ca}$	Solid-phase active material volume fraction in cathode	0.51	-
$\sigma_{s,an}$	Effective solid-phase conductivity in the anode	2.6	S m^{-1}
$\sigma_{s,ca}$	Effective solid-phase conductivity in the cathode	2.7	S m^{-1}
$i_{0,Li}$	Exchange current density for Li plating/stripping	10	A m^{-2}
α_{Li}	Transfer coefficient of Li plating reaction	0.7	-
β	Li plating reversibility factor	0.8	-
γ	Trick for oxidation of reversible Li plating	0.01	-

Summary of physics-based model governing equations, based on the original Doyle-Fuller-Newman framework. *Reproduced with author permission from the supplementary information of Ref [36], parameters are modified to reflect the present work.*

The pseudo-2D model simulates 1) liquid-phase Li-ion concentration, 2) liquid-phase potential, 3) solid-phase potential, and 4) solid-phase Li concentration. The "primary direction" is the direction normal to the anode current-collector, the "secondary direction" is the particle-level radial coordinate resolved within both electrodes. In the primary direction, the anode current collector location is denoted as "−", the anode/separator interface is denoted as "−s", the separator/cathode interface is denoted as "s+", and the cathode current collector location is denoted as "+". The primary-direction equations govern the solid-phase potential Φ_s, liquid-phase potential Φ_e, and liquid-phase concentration c_e dynamics. The liquid-phase states (Φ_e and c_e) are solved across the entire domain from − to +. The solid-phase potential Φ_s is only solved in the electrode domains (− to −s and s+ to +). The "minus" domain is referred to as the anode. The "plus" domain is referred to as the cathode. Between these two electrode domains (−s to s+) is referred to as the separator. It is important to note that while the governing equations are similar or the same between domains, the properties are *different*. For example, the Bruggeman coefficient p is used in all domains, but the Bruggeman is different in the anode domain, as compared to the separator domain, as compared to the cathode domain. As a rule-of-thumb, assume that all parameters are domain-dependent unless otherwise stated. The reader is directed to influential work by Newman and coworkers for governing equations derivations[25,66–69].

Liquid-phase concentration, c_e

The governing equation for the liquid-phase potential is solved in the primary x-direction across the entire domain (i.e., − to + face). The governing equation can be expressed compactly as

$$\frac{\partial(\varepsilon_e c_e)}{\partial t} = \nabla_x \cdot \left(D_e \varepsilon_e^{p_e} \nabla_x c_e \; - \mathbf{i}_e \frac{t_+^0}{F} \right) + \frac{3\varepsilon_s}{R_s} j,$$

where ε_e is the domain-specific electrolyte volume fraction, c_e is the concentration in the electrolyte, t is time, D_e is the domain-independent electrolyte diffusion coefficient, p_e is the domain-specific electrolyte Bruggeman coefficient, t_0^+ is the domain-independent transport number, F is Faraday's constant, R_s is the domain-specific particle radius, and j is the charge-transfer production rate. Note that the ∇_x symbols have a subscript x. This means that these gradients and divergences are taken in the primary x-direction. The electrolyte current density $\mathbf{i}_e$ is expressed as

$$\mathbf{i}_e = -\kappa_e \varepsilon_e^{p_e} \nabla_x \Phi_e \; + \; 2 \frac{\kappa_e \varepsilon_e^{p_e} RT}{F} \left(1 + \frac{\partial \, ln f_{\pm}}{\partial \, c_e} \right) (1 - t_+^0) \nabla_x ln \, c_e \, ,$$

where R is the universal gas constant, T is the temperature, κ_e is the domain-independent electrolyte conductivity, and $(\partial \, ln f_{\pm} / \, \partial c_e)$ is the domain-independent thermodynamic factor. The charge-transfer production of Li j is domain-dependent. In the separator (−s to s+) j=0. In either the anode or the cathode, j is expressed in the Butler--Volmer formulation as

$$j = \frac{i_0}{F} \left[exp\left(\frac{(1-\alpha)F(\Phi_s - \Phi_e - U_{OCP})}{RT} \right) - exp\left(\frac{-\alpha F(\Phi_s - \Phi_e - U_{OCP})}{RT} \right) \right],$$

where i_0 is the domain-specific exchange current density, α is the transference number, and U_{OCP} is the domain-specific open-circuit potential. The liquid-phase concentration c_e has no-flux boundary conditions at the − and + faces. This is expressed mathematically as

$$\mathbf{n} \cdot \nabla_x c_e|_{-,t} \; = \; 0, \qquad \text{and} \qquad \mathbf{n} \cdot \nabla_x c_e|_{+,t} \; = \; 0,$$

where **n** is the surface normal. The initial conditions are assumed to be uniform across all domains,

$$c_{\mathrm{e}}(x)|_{t=0} \;=\; c_{\mathrm{e},0}.$$

Liquid-phase potential, Φ_{e}

The liquid-phase potential is solved across the entire domain. Notably, the liquid-phase potential is commonly referred to as a "constraint equation"' because it does not have a time derivative. The liquid-phase potential governing equation can be expressed as

$$\nabla_x \cdot \mathbf{i}_e \;=\; \frac{3\varepsilon_s}{R_s}\, j\, F.$$

The boundary conditions for the liquid-phase potential are defined at the − and + face. At these boundaries, the current is set to zero. Mathematically, this can be stated as

$$\mathbf{n} \cdot \mathbf{i}_{\mathrm{e}}|_{-,t} \;=\; 0, \qquad \text{and} \qquad \mathbf{n} \cdot \mathbf{i}_{\mathrm{e}}|_{+,t} \;=\; 0.$$

Depending on the solver, this constraint equation may or may not need an initial condition. If an initial condition is required, the potential can be assumed to be uniform across the domain and be near

$$\Phi_e(x)|_{t=0} \;\approx -\, U_{OCP,an}\left(\frac{c_{s,0}}{c_{s,max}}\right),$$

where $c_{\mathrm{s},0}$ is the initial solid-phase concentration in the anode domain, and $U_{\mathrm{OCP,an}}$ is the open-circuit potential function in the anode domain.

Solid-phase potential, Φ_s

The solid-phase potential is solved in the primary direction in the anode and cathode domains. It is not resolved in the separator. The solid-phase potential dynamics can be expressed as

$$\nabla_x \cdot \left(-\sigma_s\,(1-\epsilon_{el})^{p_s}\,\nabla_x \Phi_s\right) \;=\; \frac{-3\varepsilon_s}{R_s}\, j\, F,$$

where σ_{s} is the domain-specific solid-phase conductivity, ε_s is the domain-specific solid-phase volume fraction, and p_s is the domain-specific solid-phase Bruggeman coefficient. The solid-phase potential requires boundary conditions at either end of the domain (− and +), and at the interior boundaries (−s and s+). At the − boundary, the potential is set to zero

$$\Phi_s|_{-} \;= 0.$$

At the separator boundaries, −s and s+ the flux is zero

$$\mathbf{n} \cdot \nabla_x \Phi_{\mathrm{e}}|_{-s,t} \;=\; 0, \qquad \text{and} \qquad \mathbf{n} \cdot \nabla_x \Phi_{\mathrm{e}}|_{s+,t} \;=\; 0.$$

At the + face, either the flux can be set (constant-current mode), or the potential can be specified (constant-voltage mode). Constant-current mode can be expressed as

$$\mathbf{n} \cdot \left(-\sigma_s\,(1-\epsilon_{el})^{p_s}\,\nabla_x \Phi_s\right)|_{+} \;=\; -\frac{I}{A},$$

where I is the current demanded (in Amps) and A is the current-collector geometric area. Constant-voltage mode is represented as

$$\Phi_s|_{+} \;=\; U_{CV}\,,$$

where U_{CV} is the specified constant-voltage constraint. The solid-phase potential Φ_s initial conditions are domain-specific and are not necessarily required for this algebraic constraint equation. If required, in the anode, the potential is approximately the same value as the boundary condition at the − face

$$\Phi_s|_{x\in[-,-s],t=0} \approx 0.$$

In the cathode, the potential is approximately related to the battery-level open-circuit potential

$$\Phi_s|_{x\in[s+,+],t=0} \approx U_{OCP,ca}\left(\frac{c_{s,ca,0}}{c_{s,ca,max}}\right) - U_{OCP,an}\left(\frac{c_{s,an,0}}{c_{s,an,max}}\right),$$

where U_{OCP} is the open-circuit potential function and $c_{s,0}$ is the initial solid-phase concentration. Note that extra subscripts are added to identify anode- and cathode-specific properties.

Secondary-direction, solid-phase Li concentration, c_s

The solid-phase Li concentration is resolved on the secondary *r*-axis. If it is easier to rationalize, assume that c_s is a function of *x* and *r*. However, the gradients in the *x*-direction are ignored. The solid-phase concentration is only solved for in the anode and cathode domains. These equations are not solved in the separator. The spherical governing equations for the solid-phase concentration are

$$\frac{\partial\, c_s(x,r)}{\partial t} = -\nabla_r \cdot\, (-D_s \nabla_r c_s),$$

where D_s is the domain-specific solid-phase diffusion coefficient. In spherical coordinates, this can be expanded to

$$\frac{\partial\, c_s(x,r)}{\partial t} = \frac{1}{r^2}\frac{\partial}{\partial r}\left(D_s r^2 \frac{\partial c_s}{\partial r}\right),$$

This equation requires radial boundary conditions at the center and surface of the particle. At the particle center, the symmetry condition is

$$\frac{\partial c_s}{\partial r}|_{r=0} = 0.$$

At the particle surface, the flux is specified to be related to the Butler—Volmer current

$$-D_s \frac{\partial c_s}{\partial r}|_{r=R_s} = j.$$

Finally, the domain-specific initial concentration is assumed to be uniform (within the domain) for all *x* and *r* locations

$c_s(t=0)|_{x\in[-,-s],r\in[0,R_s]} = c_{s,an,0}$, and $c_s(t=0)|_{x\in[s+,+],r\in[0,R_s]} = c_{s,ca,0}$.

Note that R_s and $c_{s,0}$ are both domain-specific.

Model parameter expressions. Table S2 documents the constant physics-based model parameters. The parameters with functional dependence are expressed below. Several of these expressions have been published before in Colclasure et al[5], and some have been modified from other works[31,36]. The electrolyte Li-ion diffusion coefficient depends on the salt concentration and temperature and can be expressed as

$$\begin{aligned} log_{10}\left(1E4\, D_e(c_e,T)\right) &= \left(-0.5688226 - \frac{1607.003}{T-(-24.83763 + 64.07366c_e)}\right. \\ &+ \left(-0.8108721 + \frac{475.291}{T-(-24.83763+64.07366c_e)}\right)c_e \\ &+ \left.\left(-0.005192312 - \frac{33.43827}{T-(-24.83763+64.07366c_e)}\right)c_e^2\right). \end{aligned}$$

In the above equation, it is assumed that c_e is in kmol m^{-3}, *T* is in K, and D_e is in m^2 s^{-1}.

The electrolyte ionic conductivity is expressed as a function of salt concentration and temperature as

$$\kappa_e(c_e,T) = c_e\left((0.0001909446\,T^2 - 0.08038545\,T + 9.00341) + (-0.00000002887587\,T^4 + 0.00003483638\,T^3 - 0.01583677\,T^2 + 3.195295\,T - 241.4638)c_e + (0.00000001653786\,T^4 - 0.0000199876\,T^3 + 0.009071155\,T^2 - 1.828064\,T + 138.0976)c_e^2 + (-0.000000002791965\,T^4 + 0.000003377143\,T^3 - 0.001532707\,T^2 + 0.3090003\,T - 23.35671)c_e^3\right),$$

where κ_e is in S m^{-1}, c_e is in kmol m^{-3}, and T is in K. The electrolyte thermodynamic factor is a function of concentration and temperature and can be expressed as

$$\left(1+\frac{\partial\, ln f_{\pm}}{\partial\, c_e}\right) = 0.54\,c_e^2\,exp\left(\frac{329}{T}\right) + 0.00225\,c_e exp\left(\frac{1360}{T}\right) - 0.341 exp\left(\frac{261}{T}\right) + 2\,,$$

where c_e is in kmol m^{-3}, and T is in K. The Li-ion transport number can be expressed as

$$t_+^0 = (-0.0000002876102\,T^2 + 0.0002077407\,T - 0.03881203)c_e^2 + (0.000001161463\,T^2 - 0.00086825\,T + 0.1777266)c_e + (-0.0000006766258\,T^2 + 0.0006389189\,T + 0.3091761),$$

where c_e is in kmol m^{-3}, and T is in K. The exchange current density for the anode is expressed as

$$i_{0,an}\left(c_{s,an}|_{r=R_{s,an}},T\right) = 0.6\,exp\left(\frac{-30E6}{R}\left(\frac{1}{T}-\frac{1}{303.15}\right)\right)c_e^{\alpha}\left(c_{s,an,max} - c_{s,an}|_{r=R_{s,an}}\right)^{\alpha}\left(c_{s,an}|_{r=R_{s,an}}\right)^{1-\alpha},$$

where $c_{s,an}$, c_e, and $c_{s,an,max}$ are in kmol m^{-3} R is in J kmol^{-1} K^{-1}, T is in K, and $i_{0,an}$ is in A m^{-2}. Thus, the pre-factor has units A m^{-2} $\cdot$ [m$^{4.5}$ kmol$_{Li^+}^{-0.5}$ kmol$_{Li,s}^{-1}$]. The exchange current density in the cathode can be expressed as

$$i_{0,ca}(x,c_e,T) = 9(16.50452829641290\,x^5 - 75.23567141488800x^4 + 124.0524690073040x^3 - 94.16571081287610x^2 + 32.49768821737960\,x - 3.585290065824760)\left(\frac{c_e}{1.2}\right)^{\alpha}\exp\left(\frac{-30E6}{R}\left(\frac{1}{T}-\frac{1}{303.15}\right)\right),$$

where $x = c_{s,ca}|_{r=Rs,ca}/c_{s,ca,max}$ is unitless, c_e is in kmol m^{-3}, T is in K, and $i_{0,ca}$ is in A m^{-2}. The anode solid-phase diffusion coefficient can be expressed as

$$D_{s,an}(T) = 3E-14\,exp\left(\frac{-30E6}{R}\left(\frac{1}{T}-\frac{1}{303.15}\right)\right)(1.5-x)^{2.5},$$

where $x = c_{s,an,avg}/c_{s,an,max}$ is unitless, where $D_{s,an}$ is in m^2 s^{-1}, R is in J kmol^{-1} K^{-1}, T is in K. The cathode solid-phase diffusion coefficient can be expressed as

$$D_{s,ca}(x,T) = 2.25 * 10^{\gamma}\exp\left(\frac{-30E6}{R}\left(\frac{1}{T}-\frac{1}{303.15}\right)\right),$$

$$\gamma = -250.9010843479270x^{10} + 2391.026725259970x^{9} - 4868.420267611360x^{8} - 83.31104102921070x^{7} + 10576.36028329000x^{6} - 12683.24548348120x^{5} + 5016.272167775530x^{4} + 982.4896659649480x^{3} - 1502.439339070900x^{2} + 472.3709304247700x^{4} - 65.26092046397090 ,$$

where $x = c_{s,ca} / c_{s,ca,max}$ is unitless, R is in J kmol^{-1} K^{-1}, T is in K, and $D_{s,ca}$ is in m^2 s^{-1}.